Effects of chamber configuration on the nanoparticle output of spark discharge generators: A combined CFD, particle tracing, and experimental

Journal of Aerosol Science 195 (2026) 106810

Contents lists available at ScienceDirect

Journal of Aerosol Science

journal homepage: www.elsevier.com/locate/jaerosci

Effects of chamber configuration on the nanoparticle output of spark discharge generators: A combined CFD, particle tracing, and experimental study

M. Bermeo [a,*,1], D. Megyeri [b,**,1], M.H. Magnusson [a], A. Kohut [b], Zs Geretovszky [b], M.E. Messing [a,c]

[a] Solid State Physics & NanoLund, Department of Physics, Lund University, Box 118, 22100, Lund, Sweden
[b] Department of Optics and Quantum Electronics, University of Szeged, Dóm sq. 9, 6720, Szeged, Hungary
[c] Department of Microtechnology and Nanoscience, Chalmers University of Technology, 412 96, Gothenburg, Sweden

ARTICLE INFO

Keywords:
Spark ablation
Nanoparticles
COMSOL simulation
CFD
Particle tracing
Residence time

ABSTRACT

Spark discharge generators (SDGs) are versatile tools for producing nanoparticles (NPs) with tailored properties. This study combines Computational Fluid Dynamics (CFD) and Particle Tracing (PT) simulations in COMSOL Multiphysics® with experimental data to investigate the effect of various chamber configurations, including inlet/outlet positioning and chamber volume on the NP output. Five geometries were tested, with results showing that shorter inlet-to-outlet distances increase the gas velocity at the electrode gap, reduce particle residence time, and lead to higher particle yields. The experimental results were consistent with the simulations after normalization to the product of spark energy and frequency, indicating only a minor dependence of output concentration on chamber volume, given that the residence time does not exceed the sparking period. Our results highlight the effectiveness of combined CFD-PT simulations in predicting and optimizing SDG performance.

1. Introduction

Spark ablation has emerged as a chemical-free technique for producing nanoparticles (NPs) with controllable morphology, size, concentration, and composition (Burtscher et al., 1982; Drdova et al., 2024; Messing, 2016; Pfeiffer et al., 2014a; Schmidt- and Ott, 2019). The inherent tunability of NPs' properties has made the use of spark ablation fundamental in research and also sparked interest in large-scale, industrial nanoparticle production applications where throughput and reproducibility are critical (Feng et al., 2015). Although spark ablation is proven to be scalable either via parallelization or increasing sparking frequency (Pfeiffer et al., 2014b), the ablation rate is relatively low on a single spark level, which highlights the importance of studying methods to improve particle generation yield.

Previous studies have explored several operational parameters to optimise the performance of a spark ablation system. The impact of different carrier gases (N_2, Ar, N_2-H_2, Ar-H_2, air), gas flow rates, electrode material, -composition, -diameter, -gap, sparking

* Corresponding author.
** Corresponding author.
E-mail addresses: marie.bermeo_vargas@ftf.lth.se (M. Bermeo), megyeri.daniel@szte.hu (D. Megyeri).
[1] These authors have contributed equally to this work.

https://doi.org/10.1016/j.jaerosci.2026.106810
Received 13 January 2026; Received in revised form 18 March 2026; Accepted 18 April 2026
Available online 22 April 2026

frequency, circuit resistance, and -capacitance on NP composition, crystal structure, size distribution, and yield was investigated (Domaschke et al., 2018; Jönsson et al., 2024; Kohut et al., 2018; Olszok et al., 2023; Schmidt- and Ott, 2019; Snellman et al., 2021; Zábojníková et al., 2025). However, while much progress has been made in optimizing the spark discharge generators' (SDG) operating parameters, relatively little attention has been given to the role of chamber geometry – such as chamber volume, electrode placement, and inlet/outlet positioning – in affecting particle output and transport efficiency.

The generation and transport of NPs in an SDG are closely linked to the flow characteristics within the chamber. Inefficient flow geometries can lead to particle losses due to deposition on the inner walls of the SDG chamber or agglomeration in stagnant zones, ultimately reducing particle yield. By contrast, optimum flow conditions in the SDG can improve particle transport to the outlet, thereby enhancing NP output. The interplay between chamber design and particle behaviour can be studied using combined Computational Fluid Dynamics (CFD) and Particle Tracing (PT) simulations. These modelling techniques allow the study of the gas flow and particle trajectories in various chamber configurations, offering a cost-effective way to complement experimental investigations.

Previous works have demonstrated the value of combining simulations and experiments to optimise the SDG performance. For example, Megyeri et al. (Megyeri et al., 2021) performed experimental measurements and CFD simulations to evaluate the effect of varying flow configurations (namely, cross-, coaxial-, and mixed flow geometries), inlet-to-outlet distances, and volumetric flow rates on the size distribution of NPs. Moreover, Han et al. (Han et al., 2012) investigated the effect of a pin-to-plate type electrode configuration on the particle size and charge distributions. However, comprehensive studies that systematically examine the influence of chamber configuration – such as different chamber shape and volume – on particle output remain scarce.

This work systematically explores the relationship between chamber geometry and NP output. We employ CFD and PT simulations to model flow behaviour, particle transport, and transmission probabilities in various SDG configurations. The simulations are conducted using COMSOL Multiphysics®, allowing us to evaluate how parameters such as inlet and outlet placement, electrode-to-inlet/outlet distance, and chamber shape and volume influence NP yield. Importantly, we complemented these simulation results with experimental studies on modified SDG chambers having different volumes and inlet/outlet configurations, thus providing an understanding of the impact of different chamber designs on the particle output.

2. Experimental methods

2.1. Spark discharge generator

A spark discharge generator – as described in more detail by Meuller et al. (Mueller et al., 2012) – was used in five different chamber configurations while keeping the rod-to-rod electrode geometry unchanged. The initial configuration consisted of a six-way cross type stainless-steel chamber (denoted as E) shown in Fig. 1 with both inlet and outlet tubes placed at 47.2 mm from the electrode surface. It was first modified to keep the chamber volume with a different inlet-to-outlet distance by adding longer inner inlets and outlets (at 10 mm from the electrode surface). In order to vary the chamber volume – while keeping the inlet and outlet positions constant – 2 to 6 tightly-fitting alumina blocks was introduced to the side ports of the chamber (please see Table 1 for details). For all the experiments, Pd rod electrodes of 3.00 mm diameter were mounted as the anode and cathode of the SDG. The Pd NPs transported in aerosol form with an N_2 carrier gas were sintered at 750 °C into fully compact particles at a constant flow rate of 1.68 L/min. Particle concentration measurements were performed using a differential mobility analyser (DMA) – custom Vienna type (Knutson & Whitby, 1975) – in conjunction with an electrometer (TSI 3086B). The DMA classifies aerosol particles according to their electrical mobility, which is directly related to their mobility diameter. During the measurements, the DMA voltage was scanned to select particles with different electrical mobilities, while the resulting particle current exiting the classifier was measured by the electrometer. The measured electrical mobility distributions were converted to particle size distributions using standard electrical mobility-diameter relationship employed in DMA measurements. To improve statistical reliability, the reported size distributions represent the average of multiple

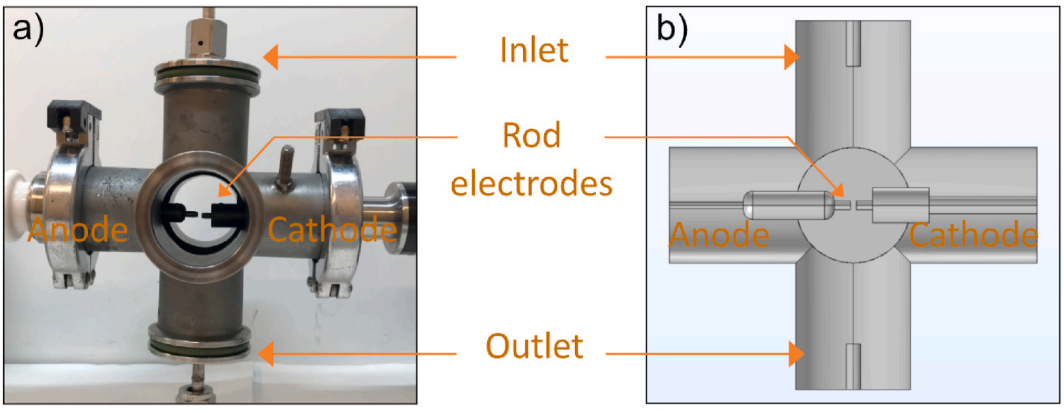

Fig. 1. Front view of SDG (a) chamber E configuration and the 2D projection of its (b) corresponding 3D model geometry used in COMSOL.

Table 1
Different SDG chamber configurations and the corresponding velocity magnitude profiles (all 2D cuts are in the y-z plane).

Item	Chamber configuration	Volume [cm^3]	3D View	Front view	Velocity profile [m/s]
E	Existing SDG [a]	401	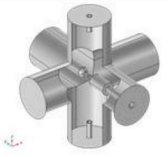	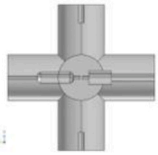	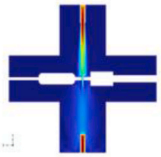
0B	0 blocks [b]	400		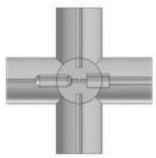	
2B	2 blocks (inlet and outlet) [b]	291	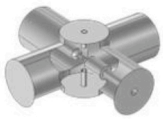	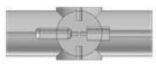	
4B	4 blocks: (inlet, outlet, anode, and cathode) [b]	185	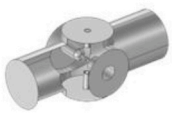		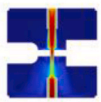
6B	6 blocks: (inlet, outlet, anode, cathode, back, and front) [b]	75.2			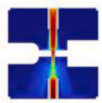

[a]The surface of the Inlet and Outlet tube are located at 47.2 mm from the electrode surface.
[b] The surface of the Inlet and Outlet tube are located at 10 mm from the electrode surface.

DMA scans performed under stable operating conditions.

The measurements were carried out under a capacitor charging current of 10 mA and using an electrode gap of 2.00 mm. All experiments were conducted under atmospheric pressure conditions.

The chamber configurations used in this study are shown in Table 1. They are named as follows: i) chamber E with inner and outlet tubes at 47.2 mm from the electrodes and no blocks, ii) a chamber with inner and outlet tubes at 10 mm from the electrodes and no blocks (0B), iii) a chamber with two blocks (2B) located at the inlet and outlet flanges, iv) a chamber with four blocks (4B) located at the inlet, outlet, anode, and cathode arms of the 6-way cross, v) and chamber with six blocks (6B) located in all the six flanges of the SDG chamber, i.e. at the inlet, outlet, anode, cathode, front, and back positions. Chamber geometries modified by the alumina blocks are sometimes collectively referred to as Bs.

2.2. COMSOL simulations

The simulations were conducted using COMSOL Multiphysics® software (COMSOL, AB.). The chamber geometries shown in Table 1, including their internal components, were precisely reproduced in digital 3D form to match the configurations used in the physical experiments to ensure dimensional consistency between the experimental and computational studies. CFD 3D simulations were performed to study the steady flow field characteristics within the chambers. To account for both laminar and turbulent cases, the Reynolds-averaged Navier-Stokes (RANS) and the continuity equations were solved simultaneously, assuming a single-phase, steady, incompressible nitrogen flow. Initially, a k-ε model was used to solve the RANS equations, and the results were later refined using the *Low Re* k-ε model (Megyeri et al., 2021). The potential thermal effect of convection on the flow field was neglected in our simulations. For further considerations on thermal effects please see the Results and discussion section.

For evaluating particle transport and distribution within the chambers, CFD simulations were complemented by PT simulations. Note that we did not attempt to simulate the particle formation process; rather, our analysis focused solely on tracking particle motion. These simulations utilized 100,000 virtual particles with a lognormal size-distribution (having identical geometrical mean and size spread as obtained from experimental measurements) released at a single event at $t = 0$ from a predefined cylindrical volume of 31.8

mm^3 located in the electrode gap (the cylinder height is identical to the spark gap with a radius equal to 1.5 times the electrode radius), representing the active particle generation zone in the SDG (Palomares et al., 2015). In the simulations, the particle yield of each investigated chamber configuration is defined by the transmission probability (TP), which is calculated as the ratio of the number of particles exiting the chamber to the number of particles initially released from the particle source (Eq. S(1)). The particle release was modelled with randomized initial positions inside the cylinder to simulate realistic conditions. To further characterize chamber configurations, we introduce another parameter, the mode of the residence time distribution (RTD), which is obtained by differentiating the cumulative number of particles exiting the chamber with respect to time. For further details, please see Fig. S1 and S2 and Eq. S(2) in the Supplementary Information (SI). Please note that the mode of the RTD will be referred to simply as residence time in the present study for convenience. The number of particles released from the source region in the simulations was increased until the transmission probability stabilized, ensuring a statistically representative particle population, which was reached for 100,000 particles. The effect of the initial number of particles on the TP and RTD was also investigated in the simulations; for further details, see Fig. S3 in the SI. Please note that the size of the particle generation zone does not affect the mode of the RTD (see Fig. S4 in the SI). It was confirmed by preliminary simulations that the only relevant force acting on the particles in the investigated size range, ranging from 4 nm to 100 nm, is the drag force, which was modelled using a standard drag coefficient. The particle's response time (i.e. the time it takes for a particle initially at rest to reach the velocity of the flow field) is in the range of microseconds, i.e., three orders of magnitude shorter than that of the typical residence time, therefore in the simulations we set the particle's initial velocity to match the velocity of the flow field at the starting point to balance computational cost. Our simulations use these initial values and assume that all spark events are identical and independent. By independence, we also refer to the particles themselves, as in the simulations we assume that the nanoparticle populations generated by successive spark discharges do not interact with each other, since investigating interparticle interactions is not the objective of this study.

3. Results and discussions

The different chamber configurations summarized in Table 1 were implemented experimentally, and the average output concentration and the size distribution of the generated particles were measured. The corresponding results are presented in Table 2. Among the tested B configurations (0B, 2B, 4B, 6B), all outperformed the E configuration in terms of output concentration. This suggests that decreasing the inlet-to-outlet distance affects the yield of the SDG, however, there is no clear tendency in the experimental data for the B geometries, i.e. the role of chamber volume and shape is unclear.

As a first attempt to understand the effect of chamber configuration on the particle yield of the SDG, CFD simulations were made at each geometry as detailed in the Experimental methods section. Table 1 (last column) and Fig. 2 present the velocity profiles of the gas flow for various SDG chamber configurations obtained from CFD simulations, characterising the flow from the edges of the inlet to the outlet for each chamber configuration. The colourmaps in Table 1 show a significant difference between the – almost identical – flow velocities of the B configurations (0B, 2B, 4B, and 6B) around the electrode gap, as opposed to a much lower intensity for the E configuration.

Fig. 2 shows the flow velocity magnitude (in m/s) of the carrier gas along the common central axis defined by the symmetry axes of the inlet and the outlet tubes for each SDG chamber configuration. The horizontal axis represents the chamber position (in mm), with the centre of the electrode gap set at 0 mm. The results show that all the B configurations exhibit nearly identical velocity profiles, which can be solely attributed to the proximity of the inlet and outlet tubes to the electrodes. In contrast, chamber E has a velocity profile characterized by the lowest overall values at every axial position. It is worth noting that very similar velocity profiles were obtained for all chamber configurations, when performing the simulations in a laminar flow regime (not shown). A distinct velocity peak is observed at the electrode gap (chamber position = 0 mm) for all configurations. This peak is the result of the constriction of the flow path between the electrodes, where the gas flow is accelerated due to the reduced cross-sectional area. The B configurations have a maximum velocity of ca. 2.7 m/s in the gap region, 1.5 times higher than that obtained for chamber E, which reaches ca. 1.7 m/s, at most. Also, a decrease in velocity is observed just before and after the electrode gap. Before the gap, the velocity decreases slightly as the flow encounters resistance and transitions into the constricted electrode gap region. After the gap, the velocity drops again as the gas flow expands towards the outlet region. These valley-peak-valley transitions may induce local turbulences that may also be reflected in particle trajectories. From the point of view of NP generation, the results obtained in the outlet region (as opposed to the inlet one) is especially important, since this is the place where most of the NPs are generated and grow. Therefore, the significantly lower velocity magnitude profile in the E geometry in the outlet region implies a much longer residence time for the particles, which increases the diffusional losses to the walls of the chamber potentially resulting in a lower particle concentration output as compared to the B configurations, as experimentally measured and shown in Table 2.

Table 2
Experimental results for the different chamber configurations. V_d and f are the discharge voltage and spark repetition frequency, respectively.

Chamber configuration	V_d [kV]	f [Hz]	Mode diameter [nm]	Total concentration [x10^7 #/cm^3]
E	2.81 ± 0.02	97.05 ± 1.14	25.18 ± 1.81	1.42 ± 0.17
0B	2.75 ± 0.35	99.26 ± 16.62	24.21 ± 2.90	1.98 ± 0.46
2B	2.91 ± 0.10	94.09 ± 3.42	26.60 ± 2.40	2.24 ± 0.79
4B	2.89 ± 0.01	93.05 ± 0.27	24.17 ± 0.80	1.95 ± 0.11
6B	2.97 ± 0.01	92.99 ± 0.31	27.14 ± 0.10	1.87 ± 0.48

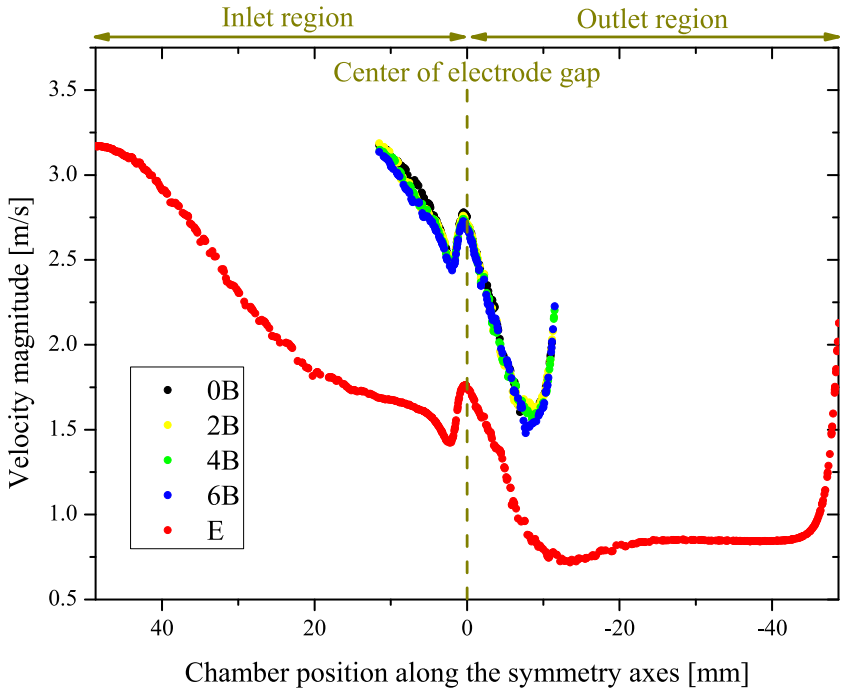

Fig. 2. Velocity magnitude of the flow field on a line segment from the inlet to the outlet for the examined SDG chamber configurations, as derived from the CFD simulated flow field.

As it was shown above, CFD flow field simulations provide a reasonable explanation on the improved particle yield observed in all the B configurations, as compared to the E configuration. However, the B configurations exhibit varying output concentrations (cf. Table 2 and Fig. 3), while characterized by very similar flow fields (cf. Fig. 2). To further investigate the source of the variation in the experimental concentration output results, PT simulations were performed for all the examined configurations. Each geometry was characterized by two quantities. We introduce transmission probability for representing the fraction of particles leaving the chamber as compared to a particle amount "generated", i.e., released in the spark gap. Furthermore, we introduce the typical residence time, which we define as the mode of the particles' residence time distribution. For further details please see the COMSOL simulations section and the SI Fig. S2. Table 3 presents the results of these simulations. The simulation of the B configurations shows very similar transmission probabilities, ranging from 91.0% to 93.3%, and nearly identical residence times, ranging from 10.2 ms to 10.4 ms. As compared to these, the E configuration resulted in a significantly higher transmission probability (99.0%) with a highly increased residence time (54.0 ms). Considering the obtained residence times, the assumptions made for PT simulations need to be revisited.

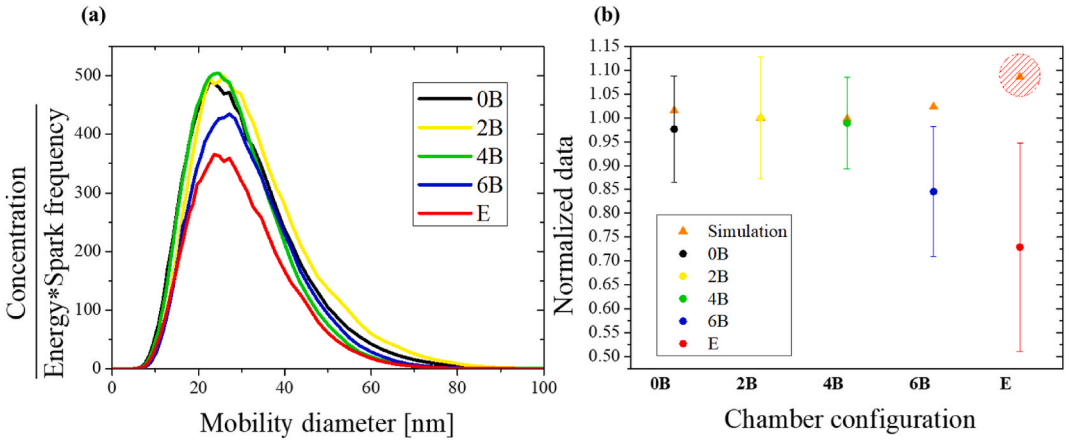

Fig. 3. The size distributions normalized to the product of spark frequency and spark energy (**a**) and the corrected concentrations normalized to the best performing modified geometry (2B) compared with simulation results (**b**). The red shaded area in the top right corner of graph (**b**) indicates the range where our simulation assumptions no longer hold. (For interpretation of the references to colour in this figure legend, the reader is referred to the Web version of this article.)

Table 3
Results of the PT simulations for various SDG chamber configurations.

Geometry	0B	2B	4B	6B	E
Transmission prob. (%)	92.6	91.2	91.0	93.3	99.0
Residence time (ms)	10.3	10.2	10.3	10.4	54.0

According to Table 2, the average time between two consecutive spark events is close to 10 ms. This means that for the B configurations most of the ablated electrode material and the NPs borne from them can leave the chamber between two consecutive spark events. For geometry E, however, the residence time is much longer (over 50 ms) than the sparking period (approx. 10 ms), meaning that consecutive NP/vapour clouds will overlap considerably, giving rise to potential effects that are not captured by the flow field-based PT simulations. Moreover, the obtained long residence time is in line with our previous qualitative picture that explains the lower measured particle yield by the increased losses associated with the longer residence of the particles inside the chamber. A note regarding the challenges in simulating the flow field and tracing the particles inside the SDG chamber is given in the SI. Regarding the high transmission probabilities, it is important to note that the PT model is exclusively based on the flow field. Additional phenomena near the electrode gap – not yet fully understood – including electric field effects, temperature gradients, and particle formation processes, may exert a significant influence that competes with the fluid flow, potentially representing a substantial source of model discrepancy. For instance, in regimes where lower velocities occur (such as configuration E), the electric field may significantly compete with drag forces, leading to a substantial reduction in transmission probability. Conversely, at higher velocities (configurations Bs), drag forces become the dominant factor, rendering other effects negligible.

Temperature gradients generated during spark events may also affect the early stages of particle formation, particularly in the vicinity of the electrode gap where localized heating occurs which consequently can influence the resulting size distribution. To ensure that the simulated particle population reflects the experimentally measured particles, the lognormal size distribution used as input in the particle tracing simulations was taken directly from experimental measurements, as detailed in the Experimental Methods section. The thermal gradients associated with the spark discharge evolve on the microsecond time scale and remain largely localized in the vicinity of the electrode gap (Kohut et al., 2017). By contrast, the particle residence times in the chamber are on the order of milliseconds (~10-50 ms), as reported in Table 3. This difference of several orders of magnitude suggests that, under the operating conditions investigated here, the overall flow dynamics are primarily governed by the carrier gas flow rather than buoyancy-driven convection. Consequently, the simulations focus on the carrier gas flow field, while thermal convection effects are not explicitly included. A more detailed discussion of the convection effects is provided in the SI. Further systematic studies will be required to elucidate the complex multiphysics interactions occurring simultaneously in the SDG.

As it was pointed out above, for the B configurations the typical residence time does not exceed the sparking period, hence consecutive sparks are correctly assumed to be independent, therefore the PT simulation results can be considered reliable. However, the simulations assume that every single spark event generates a constant number of initial particles, a fraction of which will leave the chamber. So the above defined transmission probability is directly proportional to the particle yield. Assuming that spark events are independent, one can calculate the output concentration per spark from the experimental results. However, as evidenced by Table 2, electrical parameters slightly vary with different configurations, affecting the initial particle concentration. To correct for the variations in particle yield due to the variation in spark energy and spark frequency, we divided the measured concentrations by the product of the spark frequency (f) and the spark energy (E) stored in the capacitor, i.e., $fE = fCV_d^2/2$, where C is the capacitance of the discharge circuit and V_d is the discharge voltage.

Fig. 3a shows the corrected size distributions for all modified chamber configurations. It is evident, that – after correction – every B configuration behave very similarly, and only configuration 6B is exhibiting somewhat lower particle yield. Fig. 3b compares the corrected experimental concentrations normalized to the output of the best performing configuration (which is 2B) along with the simulation results normalized to the transmission probability of the same configuration. Two conclusions can be drawn from these representations: *i)* the essentially constant particle yield predicted by the PT simulations for the modified, B configurations is in good agreement with the experimental results, after correcting the latter to the varying spark energy and frequency, and *ii)* for the 6B configuration, even the corrected experimental output is significantly lower than that of the simulated one. This suggests that the change of the chamber configuration not only affects the particle yield via the modification of the flow field, but additional effects unrelated to the flow must be taken into account. In case of the 6B configuration all the chamber walls are located the closest to the spark gap (see Table 1). This suggests that the smaller experimental yield and the largest deviation from the simulations observed at geometry 6B is due to increased losses to the walls. Since spark plasmas produce charged particles (Tabrizi et al., 2008), it is plausible to assume that the electric field – associated with the continuous charging and oscillatory discharging cycles of sparking – may also alter the transmission probability, and it is responsible for the deviation of experimental and simulation observations. The simulation of electric field in the vicinity of the electrode gap was not implemented in the present COMSOL code. Nevertheless, our combined experimental and CFD results have some important implications regarding the chamber design of SDGs. It was shown that the particle yield can be increased by decreasing the inlet-to-outlet distance up to a point, where the typical residence time does not exceed the sparking period, which is determined by the spark repetition rate. At this inlet-to-outlet distance, it was shown that the chamber volume can be decreased more than two times before potential wall-related losses start to emerge and modify the particle yield. It has been suggested recently that limiting the volume available for the ablation plume of the spark plasma is beneficial for achieving more uniform spark mixing (Kohut et al., 2025), and our present results show that this limitation can be achieved in a relatively wide range without sacrificing the particle yield.

4. Conclusions

This study investigates the impact of different chamber configurations on nanoparticle output in an SDG using a combination of Computational Fluid Dynamics (CFD) and Particle Tracing (PT) simulations which were verified using experimental measurements. The results demonstrated that the chamber geometry significantly influences flow dynamics, particle residence time, and, ultimately, NP size distribution. Five chamber configurations were investigated, the commonly used geometry (called E) served as the basis of comparison, which was gradually modified both in terms of inlet-to-outlet distance and overall chamber volume (the modified geometries called 0B, 2B, 4B, and 6B). Experimental results showed that configuration E produced the lowest particle yield, which improved at every modified configuration tested here. CFD simulations revealed that the modified chamber configurations exhibit higher velocity profiles compared to the E configuration, particularly at the electrode gap, due to the shortened inlet-to-outlet distances. The typical residence time obtained for the E geometry was five times longer than the sparking period, meaning that the particles are affected by consecutive sparking events – and the associated flow field, electric field, and shock wave effects – qualitatively explaining its poor experimental yield. For the modified configurations the residence time was short enough to ensure that most of the ablated electrode material and the particles generated by a single spark can leave the chamber before the next spark occurs, therefore PT simulations could be performed. The comparison between the residence time and the time between consecutive sparks clearly highlights the limitations of our simulation approach. The simulation of these B configurations resulted in very similar particle transmission probabilities, which were in line with the experimental results after normalizing the measured particle concentrations to unit spark energy and frequency. The good agreement between the simulations and experiments provides insight into the transport of NPs moving in a steady flow field inside an SDG, which can be modelled by considering only the drag force acting on the particles. We have also concluded that particle yield can be increased by decreasing the residence time to around the sparking period, beyond which point the impact of the chamber volume on particle yield was found to be marginal. Our results show that the modelling approach presented here provides a reliable way to design and optimise an SDG configuration. Thus, future work could explore other geometries to improve particle output efficiency.

CRediT authorship contribution statement

M. Bermeo: Writing – review & editing, Validation, Investigation, Data curation. **D. Megyeri:** Writing – review & editing, Writing – original draft, Validation, Methodology, Data curation. **M.H. Magnusson:** Supervision. **A. Kohut:** Writing – review & editing, Supervision. **Zs Geretovszky:** Supervision. **M.E. Messing:** Supervision.

Declaration of competing interest

The authors declare that they have no known competing financial interests or personal relationships that could have appeared to influence the work reported in this paper.

Acknowledgements

This work was supported by the Swedish Foundation for Strategic Research (Grant No. FFL18-0282), the European Union's Horizon 2020 research and innovation programme under the Marie Sklodowska-Curie grant agreement No. 945378 and by the National Research, Development and Innovation Fund of Hungary (under grants no. EKÖP-24-4-SZTE-653, TKP2021-NVA-19, and K 146733) and by the University of Szeged Open Access Fund, Grant ID: 8362. A. Kohut received a Bolyai Research Scholarship from the Hungarian Academy of Sciences (BO/00444/25).

Appendix A. Supplementary data

Supplementary data to this article can be found online at https://doi.org/10.1016/j.jaerosci.2026.106810.

Data availability

Data will be made available on request.

References

Burtscher, H., & Schmidt-Ott, A. (1982). Enormous enhancement of van der Waals forces between small silver particles. *Physical Review Letters, 48*(21), 1734. https://doi.org/10.1103/PhysRevLett.48.1734

Domaschke, M., Schmidt, M., & Peukert, W. (2018). A model for the particle mass yield in the aerosol synthesis of ultrafine monometallic nanoparticles by spark ablation. *Journal of Aerosol Science, 126*, 133–142. https://doi.org/10.1016/j.jaerosci.2018.09.004

Drdova, S., Gao, M., Sambalova, O., Pauer, R., Zhou, Z., Dimitriadou, S., Schmidt-Ott, A., & Wang, J. (2024). Precursor- and waste-free synthesis of spark-ablated nanoparticles with enhanced photocatalytic activity and stability towards airborne organic pollutant degradation. *Environmental Science: Nano, 11*(3), 1023–1043. https://doi.org/10.1039/d3en00348e

Feng, J., Biskos, G., & Schmidt-Ott, A. (2015). Toward industrial scale synthesis of ultrapure singlet nanoparticles with controllable sizes in a continuous gas-phase process. *Scientific Reports, 5*(1), Article 15788. https://doi.org/10.1038/srep15788

Han, K., Kim, W., Yu, J., Lee, J., Lee, H., Woo, C. G., & Choi, M. (2012). A study of pin-to-plate type spark discharge generator for producing unagglomerated nanoaerosols. *Journal of Aerosol Science, 52*, 80–88. https://doi.org/10.1016/j.jaerosci.2012.05.002

Jönsson, L., Snellman, M., Eriksson, A. C., Kåredal, M., Wallenberg, R., Blomberg, S., Kohut, A., Hartman, L., & Messing, M. E. (2024). The effect of electrode composition on bimetallic AgAu nanoparticles produced by spark ablation. *Journal of Aerosol Science, 177*, Article 106333. https://doi.org/10.1016/j.jaerosci.2023.106333

Knutson, E. O., & Whitby, K. T. (1975). Aerosol classification by electric mobility: Apparatus, theory, and applications. *Journal of Aerosol Science, 6*(6), 443–451. https://doi.org/10.1016/0021-8502(75)90060-9

Kohut, A., Ludvigsson, L., Meuller, B. O., Deppert, K., Messing, M. E., Galbács, G., & Geretovszky, Z. (2017). From plasma to nanoparticles: Optical and particle emission of a spark discharge generator. *Nanotechnology, 28*(47), Article 475603. https://doi.org/10.1088/1361-6528/aa8f84

Kohut, A., Villy, L. P., Ajtai, T., Geretovszky, Z., & Galbács, G. (2018). The effect of circuit resistance on the particle output of a spark discharge nanoparticle generator. *Journal of Aerosol Science, 118*, 59–63. https://doi.org/10.1016/j.jaerosci.2018.01.011

Kohut, A., Villy, L. P., Jönsson, L., Megyeri, D., Galbács, G., Messing, M. E., & Geretovszky, Z. (2025). Gold–silver alloy nanoparticle formation via spark ablation: The dynamics of material mixing. *Nanoscale Advances, 7*, 3322–3330. https://doi.org/10.1039/D4NA01076K

Megyeri, D., Kohut, A., & Geretovszky, Z. (2021). Effect of flow geometry on the nanoparticle output of a spark discharge generator. *Journal of Aerosol Science, 154*, Article 105758. https://doi.org/10.1016/j.jaerosci.2021.105758

Messing, M. E. (2016). The advantages of spark discharge generation for manufacturing of nanoparticles with tailored properties. *Journal of Green Engineering, 5*(3–4), 83–96. https://doi.org/10.13052/jge1904-4720.5346

Mueller, B. O., Messing, M. E., Engberg, D. L. J., Andersson, S. B., & Deppert, K. (2012). Review of spark discharge generators for production of nanoparticle aerosols. *Aerosol Science and Technology, 46*(11), 1256–1270. https://doi.org/10.1080/02786826.2012.705448

Olszok, V., Bierwirth, M., & Weber, A. P. (2023). Creation of gases with interplanetary oxygen concentration at atmospheric pressure by nanoparticle aerosol scavengers: Implications for metal processing from nm to mm range. *ACS Applied Nano Materials, 6*(3), 1660–1666. https://doi.org/10.1021/acsanm.2c04585

Palomares, J. M., Kohut, A., Galbács, G., Engeln, R., & Geretovszky, Z. (2015). A time-resolved imaging and electrical study on a high current atmospheric pressure spark discharge. *Journal of Applied Physics, 118*(23), Article 233301. https://doi.org/10.1063/1.4937729

Pfeiffer, T. V., Feng, J., & Schmidt-Ott, A. (2014a). New developments in spark production of nanoparticles. *Advanced Powder Technology, 25*(1), 56–70. https://doi.org/10.1016/j.apt.2013.12.005

Pfeiffer, T. V., Feng, J., & Schmidt-Ott, A. (2014b). New developments in spark production of nanoparticles. *Advanced Powder Technology, 25*(1), 56–70. https://doi.org/10.1016/j.apt.2013.12.005

Schmidt-Ott, A. (Ed.). (2019). *Spark ablation: Building blocks for nanotechnology* (1st ed.). CRC Press.

Snellman, M., Eom, N., Ek, M., Messing, M. E., & Deppert, K. (2021). Continuous gas-phase synthesis of core–shell nanoparticles via surface segregation. *Nanoscale Advances, 3*(11), 3041–3052. https://doi.org/10.1039/d0na01061h

Tabrizi, N. S., Ullmann, M., Vons, V. A., Lafont, U., & Schmidt-Ott, A. (2008). Generation of nanoparticles by spark discharge. *Journal of Nanoparticle Research, 11*(2), 315. https://doi.org/10.1007/s11051-008-9407-y

Zábojníková, N., Vretenár, V., Híveš, J., & Němec, T. (2025). Carrier gas-driven compositional variations of platinum-tungsten nanoparticles generated by spark ablation. *Journal of Aerosol Science, 185*, Article 106538. https://doi.org/10.1016/j.jaerosci.2024.106538